

As-Continuous-As-Possible Ceramics Printing for Shell Models

FANCHAO ZHONG, Shandong University

YONGLAI XU, Shandong University

HAISEN ZHAO, IST Austria, University of Washington and Shandong University

LIN LU, Shandong University

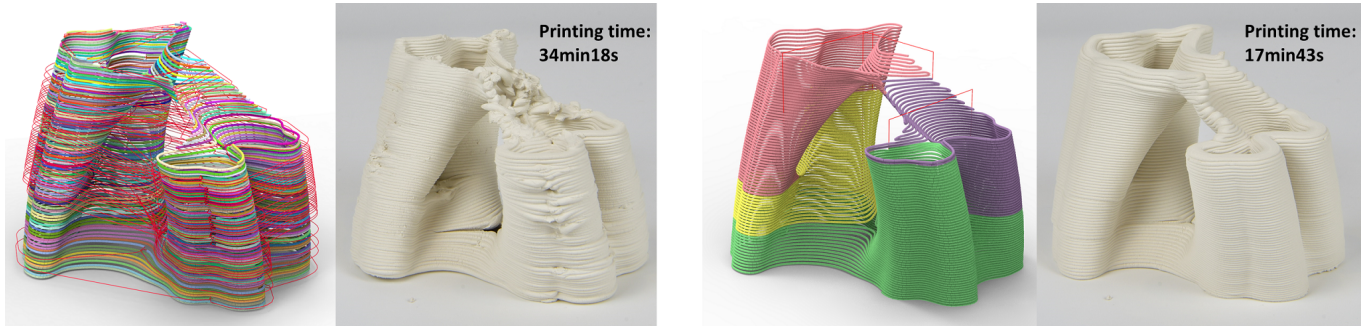


Fig. 1. Our framework significantly improves fabrication efficiency and product quality of shell models with *as-continuous-as-possible* ceramics printing. A novel geometric criterion “one-path patch” (OPP) is proposed to decompose the input shell into a minimal number of continuous printing patches with flat and curved paths. Compared with the 195 disconnected printing toolpaths with only flat slicing layers (left) generated by Ultimaker Cura software (different colors indicate each connected path, red lines represent the transfer moves), our framework produces 4 continuous deposition paths together with flat and curved slicing layers, realizing much better printing quality (right) and extremely efficient fabrication process (34.3 mins vs 17.7 mins).

We propose a novel computational framework for fabricating thin shell models on an extrusion-based Cartesian 3D printer with the clay material. Extrusion-based ceramics printing involves several inevitable challenges to achieve acceptable print quality, including continuous toolpath with the minimal number of transfer moves, separation of non-model and model structures, etc. Inertia of the extruded material may damage the surface quality during transfer moves. The viscosity also makes support material hard to remove. These challenges even increase for thin shell surfaces, as both sides are of visual significance, making it impossible to hide any intermediate structures in the interiors. To conquer these challenges, we adopt a curved layer scheme for ceramics printing. Then we introduce an original criterion “one-path patch” (OPP), for representing a shell surface patch that can be traversed in one path in the context of curved layer printing considering fabrication constraints. We propose a bottom-up OPP merging procedure for decomposing the given shell surface into a minimal number of OPPs and generating the “as-continuous-as-possible” (ACAP) toolpath. Furthermore, we customize the path planning algorithm with a decoupled orientation and support structures computation method. Results demonstrate that our ACAP algorithm prints shell models with both efficiency and surface quality.

Authors’ addresses: Fanchao Zhong, fanchao98@gmail.com, Shandong University; Yonglai Xu, xyliyriwi@gmail.com, Shandong University; Haisen Zhao, haisen.zhao@ist.ac.at, IST Austria, University of Washington and Shandong University; Lin Lu, llul@sdau.edu.cn, Shandong University.

Permission to make digital or hard copies of all or part of this work for personal or classroom use is granted without fee provided that copies are not made or distributed for profit or commercial advantage and that copies bear this notice and the full citation on the first page. Copyrights for components of this work owned by others than ACM must be honored. Abstracting with credit is permitted. To copy otherwise, or republish, to post on servers or to redistribute to lists, requires prior specific permission and/or a fee. Request permissions from permissions@acm.org.

© 2022 Association for Computing Machinery.

0730-0301/2022/1-ART \$15.00

<https://doi.org/10.1145/nnnnnnn.nnnnnnn>

CCS Concepts: • **Computing methodologies** → **Shape modeling**; *Graphics systems and interfaces*;

Additional Key Words and Phrases: Toolpath planning, shell models, ceramic printing

ACM Reference Format:

Fanchao Zhong, Yonglai Xu, Haisen Zhao, and Lin Lu. 2022. As-Continuous-As-Possible Ceramics Printing for Shell Models. *ACM Trans. Graph.* 1, 1 (January 2022), 15 pages. <https://doi.org/10.1145/nnnnnnn.nnnnnnn>

1 INTRODUCTION

Ceramics printing has been gaining both industrial and academic interests in recent years. As a natural material, clay is environmentally friendly and durable; thus, ceramic products are ubiquitous in construction, housing, consumer goods, etc. A feasible and cost-effective manufacturing technique for clay is direct ink writing (DIW), an extrusion method using a filament of a highly viscous paste. DIW employs a Cartesian 3D printing framework, the same architecture with fused deposition modeling (FDM), but with a larger opening nozzle that provides more material extrusion efficiency for high viscosity clay than thermoplastics [Chen et al. 2019b].

As the most popular clay expression form, shell models like potteries have developed since the Stone Age. Possessing featured functionalities like lightweight and effective thermal conductivity, shell models are widely used in oil and gas, aerospace, and craft industries [Bhatt et al. 2020]. In extrusion-based 3D printing, shell models are of high fabrication efficiency compared to solid ones.

Continuity of the toolpath plays a vital role in the quality of extrusion-based 3D printed objects. The continuity of ceramic 3D printing with clay is even more crucial due to a large amount of semi-liquid pastes during deposition and thus the artifacts caused



Fig. 2. Left: strictly-continuous path generated by [Hergel et al. 2019] but need redundant non-model structure to connect disconnected model components (the upper part of this model). Since this method only handles solid models, we slightly thicken the original shell model into a valid volume. Right: our ACAP toolpath is fully continuous using curved layers without extra path.

by transfer moves. [Hergel et al. 2019] recently proposed a path generating method tailored to extrusion-based ceramics printing, which produces strictly continuous deposition paths that eliminate transfer moves. It works well on closed surfaces, i.e., contours in each layer are all closed, such that bridges or interior support structures are "hidden" inside the shape. However, it cannot be easily adopted for shell models. There is no interior or exterior for shell models, and both sides are of visual significance, making it impossible to hide any intermediate structures. Besides, multiple curvy segments exist in one layer. Open curves have two endpoints and thus increase double contact points between the non-model structure and model structure, referring to Figure 2.

Curved layers manufacturing is regarded as an effective method for removing the stair effects of flat layers [Etienne et al. 2019] and improving the strength through aligning filaments along the directions with large stresses of the part [Fang et al. 2020]. It has been adapted to multi-axis printing platforms to strengthen the toolpath continuity for clay or concrete; however, it has never worked on the standard 3-axis platforms.

Adopting the curved layers scheme for Cartesian 3D printing with clay faces two more constraints from fabrication besides continuity. First, the layer thickness is adjustable but bounded by the extrusion amount. Second, the slope of the curved toolpath cannot be too steep. The reason is that the collision between the nozzle and printed model must be considered as the extruded clay paste does not dry instantly.

As shown in Figure 3, suppose that we sample dense points on the shell model. Due to the additive manufacturing principle, they have dependency constraints, i.e., a certain point must be printed after some prior points. Considering the fabrication constraints, a sample point has a limited set of possible successors. Thus, the path planning problem can be regarded as a precedence constrained

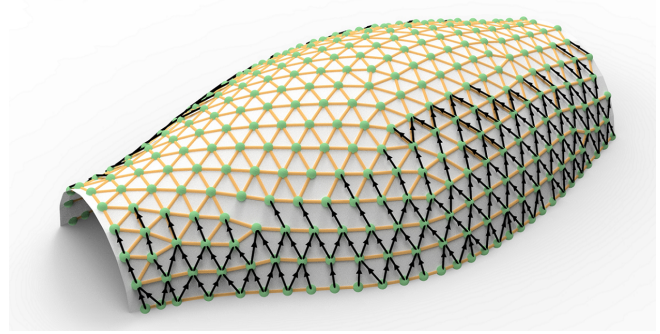


Fig. 3. PC-MPC formulation: the orange non-directed edges represent that two nodes can be continuous printing without order restriction and violating the slope angle constraint, the black directed edges demonstrate the dependency constraints between nodes (the forward node must be printed before the backward node).

minimum path cover problem (PC-MPC), which is equivalent to a classical NP-hard problem (PC-TSP, see more details in Appendix A).

Restrict the printing to flat layers, this problem can also be expressed PC-TSP. Efforts in the literature have been made to approximated solutions on solving this problem to minimize the wasted motion and thus the overall fabrication time [Lensgraf and Mettu 2017, 2018; Yoo et al. 2020].

The goal of this paper is to optimize the quality of the ceramic printed shell models. In addition to transfer moves, the contact removal artifacts caused by the support structures is another critical factors of fabrication quality. Support structures fabricated with the same material as clay make it extremely hard to remove without introducing a detrimental effect on the surface quality. We fabricate the intact model and support structures separately and add a membrane between the two parts to eliminate the contact removal artifact. Through this decoupling strategy, we can deal with the cases that the support structures are on the ground. Then, we target producing the as-continuous-as-possible toolpath for shell models, such that the number of transfer moves is minimized. Our key idea is to involve curved layers fused deposition modeling (CLFDM) [Chakraborty et al. 2008] into ceramics printing, and propose a "one-path patch" (OPP) criterion to represent a surface patch that can be printed in a continuous toolpath, in combined flat and curved layers. We propose a bottom-up OPP merging algorithm for decomposing the given shell model into a minimal number of OPPs and generate the "as-continuous-as-possible" (ACAP) toolpath.

With respect to a printing direction, a manifold surface patch is an OPP, iff 1) there exists a set of slicing layers (flat or curved) where each layer approximated orthogonal to the printing direction intersects the patch resulting of a single segment or contour; 2) the resulting intersected segments/contours satisfies the ceramics printing constraints (slope angle and layer thickness constraints), as shown in Figure 4 (In the paper we deliberately choose a low-resolution layer height to make the printing paths more visible).

This paper makes the following contributions:

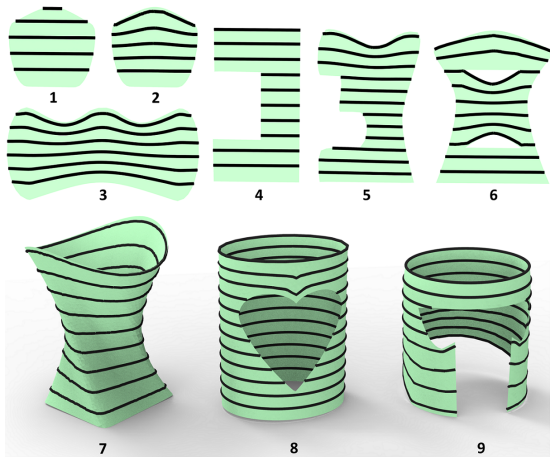


Fig. 4. Illustration of OPP patches which can be printed in a single toolpath generated from flat slicing layers (1,4), curved slicing layers (2,3,5,7), or combined flat and curved layers (6,8,9). One OPP patch can be sliced with different strategies (1,2).

- We provide a novel computational framework for printing shell models on a standard 3-axis extrusion-based ceramics printing platform.
- We introduce an original, fabrication constraints-aware, criterion “one-path patch” (OPP) for representing a shell surface patch that can be printed in one path in the context of both flat layer and curved layer printing scheme.
- We propose an optimization algorithm for decomposing the given shell surface into minimal number of OPPs and generating the “as-continuous-as-possible” (ACAP) toolpath, considering fabrication constraints.
- A decoupled support structures generation method that separates the non-model and model structures fabrication stages, avoiding the artifacts raised in support removal.

2 RELATED WORK

Ceramic printing. Additive manufacturing (AM) of ceramic materials has attracted heightened attention in recent years [Chen et al. 2019b; Zocca et al. 2015]. It would reduce both processes and resources required to produce geometrically complex shapes in the traditional ceramics industry, and thus nurture new ideas or applications in architectural decorations [Chan et al. 2020], arts, etc. Researchers are also developing and tailoring advanced engineering ceramics, such as metal oxides, carbides, and nitrides, to specific engineering demands [Peng et al. 2018]. In this paper, we take clay as the material and hereby DIW printing technique. Existing work mainly focuses on studying formulations of the water-to-clay ratios and some additives, and physical analysis on the sintered models in terms of compression, thermal stability, etc. [Ordoñez et al. 2019; Revelo and Colorado 2018].

Even though the slicing and toolpath planning for DIW ceramics printing share both constraints and objectives with FDM, it possesses additional constraints due to the viscosity of clay, which is attracting the attention of researchers. Recent attempts consider

the path planning for closed model [Hergel et al. 2019], integrated modeling and path generation for relatively simple shapes [Zhong et al. 2020], and stability enhancement for shell models [Xing et al. 2021]. While for general shell models, there are still no effective path planning methods.

Slicing and Path planning. In AM, the slicer is used for converting a model to toolpaths. Existing slicing algorithms divide the model as a stack of flat layers by geometric operations. [Lensgraf and Mettu 2016, 2017, 2018; Yoo et al. 2020] proposed a series of optimization algorithms to minimize the total *extrusionless travel distance* (wasted motion or print time) in the space of feasible toolpaths. Although this is only for flat layers, We share similar precedence constraints. In contrast, we define the OPP criterion, reform the optimization in a more compact dependency graph, and gain a more efficient optimization framework. For most cases, we can achieve the optimal results rather than approximated ones. Many efforts have been made to optimize the toolpath in terms of continuity, filling rates, and mechanical properties [Xia et al. 2020; Zhai and Chen 2019; Zhao et al. 2016]. [Hornus et al. 2020] propose a variable-width contouring technique that further optimizes the filling density. [Hergel et al. 2019] present a method for generating strictly-continuous, self-supporting deposition paths for extrusion-based ceramic printing, performing nicely on watertight geometric models. However, this method cannot apply to shell models.

Curved layers printing. Compared with traditional flat layers, curved layers contain dynamic z-values within individual layers and have excellent properties in AM. Such as alleviating the staircase effect, improving surface smoothness, strengthening the printing model and reducing printing time. The first discussion about curved layers is called CLFDM [Chakraborty et al. 2008], which allows continuous change of the z-value within individual layers. Afterwards, [Allen and Trask 2015; B.Huang and S.Singamneni 2012; Llewellyn-Jones et al. 2016] perform physical experiments with traditional printer to demonstrate these properties. [Ezair et al. 2018] presents an algorithm that generates covering curves based on geometric characteristics of a given volume. [Etienne et al. 2019] takes a different approach that optimizes a parameterization to obtain smooth surface tops. The produced toolpaths are mapped back into the initial domain without requiring splitting or re-ordering. We apply this method in our curved OPP merging. Recently, researchers have applied curved layers printing on multi-axis printers. With the help of additional DOF, [Dai et al. 2018; Xu et al. 2019] design curved toolpath to fabricate solid models in a support-free way. [Chen et al. 2019a] present a new CLFDM slicing algorithm that allows variable thickness layers. [Fang et al. 2020] introduce a field-based optimization framework to generate curved layers for reinforcing the mechanical strength of 3D printed models. However, multi-axis printing is not friendly to clay, as it does not dry instantly and might collapse when the orientation changes.

Fabrication of thin shells. Fabricating thin shells is gaining increasing attention as it accelerates the fabrication time compared to closed models and lightweight shell models are of wide applications. This advantage is further enhanced when fabricating viscous slurries, like clay and concrete, with large extrusion amount and fast

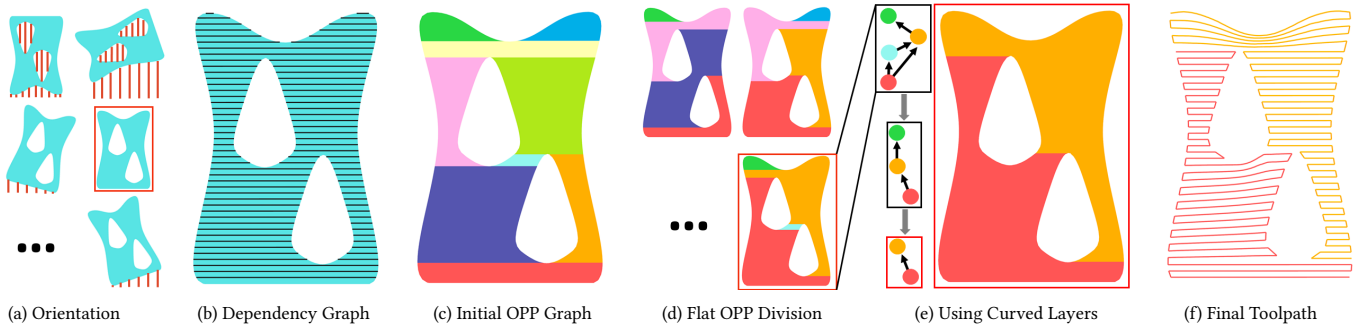


Fig. 5. Overview of the ACAP algorithm. Given a shell surface, we first determine the optimal orientation with an evaluation function (a). Then we slice horizontally along the Z-axis, build the dependency graph G_{depend} (b) where each node represents a *segment* or *contour* and each edge represents the dependency of two nodes. Cluster nodes based on the dependency relationship, obtain graph G_{init} (c). Next, we propose a novel search algorithm to solve PC-MPC to merge nodes, each optimal solution corresponds to an OPP graph G_{OPP} (d). For each one, iteratively merge nodes using curved layer (e), note that all paths meet slope angle and thickness constraints. At this point, we own a set of candidates G_{OPP} , then select the one with the least number of nodes. Finally, we generate the toolpath for each OPP (f).

deposition rate. For shell models, the continuity of material deposition is more critical due to the apparent artifacts caused by transfer moves. Most works in the literature adopt multi-axis platforms and incorporate curved layers for printing shells. [Mitropoulou et al. 2020] present a method to design non-planar layered print paths for robotic FDM printing of single-shell surfaces. [Bhatt et al. 2020] propose the layer slicing and toolpath planning algorithm to build thin shell parts on a 3-DOF build-platform and a 3-DOF extrusion tool. Printing concrete shells is attracting interests in the interdisciplinary area of digital fabrication and architecture. [Burger et al. 2020] use the single-shell as molds for concrete casting. [Anton et al. 2019] propose a design tool for producing bespoke concrete columns and involve curved layer for continuous extrusion. [Bhooshan et al. 2020] also emphasize on interactively shell modeling and integrate modeling with toolpath generation.

Decomposition for fabrication. Many efforts have been focused on model decomposition for fabrication. Objectives for model decomposition include fabricating the model that satisfy the constraint, improving surface quality, saving or avoiding support structures, and reducing printing time. [Luo et al. 2012] propose a solution to decompose the model into smaller parts that every part can fit the printing platform. In addition to considering the criterion of printing volume, structural soundness and aesthetics are their decomposition objectives. For improving surface quality, [Hildebrand et al. 2013] generate a partition and compute the optimal slicing direction for subparts. [Hu et al. 2014] decompose a given shape into as few approximate pyramidal parts as possible. Their motivation is that pyramidal shapes are well suitable for fabrication. [Vanek et al. 2014; Wei et al. 2018] decompose shell models into small parts to save the support material and reduce the printing time. A manual assembly process is required after printing all shells. Also, to avoid supporting materials, [Wu et al. 2017, 2020]’s decomposition approaches consider the collision-free constraint and sequence of printing. They printed models in a multi-DOF 3D printing system so that manual assembly is not required. [Herholz et al. 2015; Muntoni et al. 2018] decompose general three-dimensional geometries to

satisfy the height field constraint. To minimize the number of cutter setups for finish-stage machining in CNC, [Zhao et al. 2018] develop an algorithm to perform surface decomposition with the accessibility constraint. The above methods did not consider the continuity of the printing path as a criterion for model decomposition. It is worth mentioning that [Mahdavi-Amiri et al. 2020] propose carvability criteria for continually carving a connected domain, which requires both visibility and monotonicity. However, they did not take curved slicing layers into account. In such situation, the key difference between our OPP criterion and carvability is that OPP does not require visibility but support curved layering fabrication.

3 OVERVIEW

Input a thin shell model M , we first determine an optimal printing orientation by evaluating the flatten area and support structure volume (subsection 4.1), while considering the support structure constraint (subsection 3.1). With the result orientation, the following steps aim to achieve maximal path continuity, that is, decompose the model into as few (One-Path-Patch) OPPs as possible considering the path layer thickness constraint and slope angle constraint (subsection 3.1). The formulation of OPP is detailed in subsection 3.2.

As a PC-MPC problem, such decomposition is NP-hard to propose an efficient solution easily. We propose a bottom-up merging procedure to convert the PC-MPC problem into a much more tractable combinatorial optimization problem. The basic idea is to apply the flat-layer based merging (subsection 4.2, subsection 4.3) then the curved-layer based merging (subsection 4.4). Finally, carry out the path planning for each OPP following with an post optimization process to improve the path smoothness and spacing (subsection 4.5). Our algorithm pipeline is illustrated in Figure 5.

3.1 Fabrication constraints

We mainly consider three fabrication constraints in this work. The first bounds a feasible range of layer thickness. The second is to avoid collision between the extrusion device (nozzle, extruder and carriage) and the already printed parts while operating toolpath

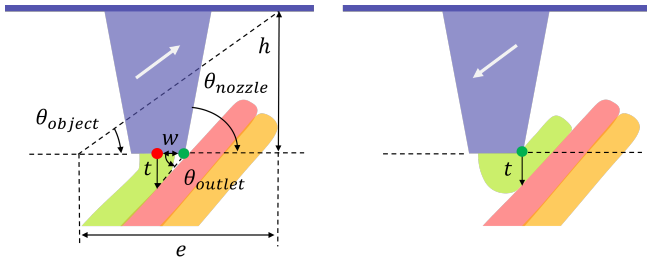


Fig. 6. Slope angle constraint of curved path: the cross section of nozzle is a trapezoid. θ_{nozzle} indicates the angle between the nozzle tip and the horizontal. $\theta_{object} = \tan^{-1} \frac{h}{e}$, where h is the vertical distance between carriage and nozzle tip and e is the maximum XY extent of the already printed object. $\theta_{outlet} = \tan^{-1} \frac{t}{w}$, where w is radius of nozzle tip. t represents a reference layer thickness (we take the average of our layer thickness range $t = 1.5mm$). (left) and (right) represent the situation when going uphill and downhill respectively. For our testing printer, $w=2.6mm$, $h=90.0mm$.

from curved layers. The third describes the geometric requirement for the decoupling fabrication strategy of the intact model and support structures.

Thickness constraint. Affected by the fluidity of clay, too small layer thickness would cause the layers squeezed together and such over-stacking effect results in bristle artifacts on the surface (see inset Figure). While too large thickness results in under-stacking and the adjacent layers are not well bonded. We use t_{min} and t_{max} to represent the minimum and maximum layer thickness. A thickness gradient test from 0.2mm to 4.5mm is produced where we take $t_{min} = 0.5mm$ and $t_{max} = 2.5mm$ for our results.



Slope angle constraint. For general 3-axis printers, the collision constraint has been modeled as an inverted cone to forbid already printed parts entering [Etienne et al. 2019]. A local slope angle constraint for the printing paths is extracted from the forbidden cone as $\theta_{max} = \min(\theta_{nozzle}, \theta_{object})$ (see Figure 6 for the detailed formulation). We propose to extend their formulation to ceramics printing. In the original model, the printer is simplified as a pointed conical nozzle by overlooking the flat outlet of the nozzle part. For ceramics printing, such nozzle outlet is always too large to be ignored (the outlet diameter is 5.2mm in our experiments). We model the nozzle outlet as an inverted trapezoid to avoid local collision from the nozzle outlet (see Figure 6).

We make an interesting observation that the possible collision differently when going uphill and downhill. See Figure 6, when going uphill (left), since the point on the right side of outlet (green dot) is closest to the layer printed below, it may collide first, which can be avoided by restricting the path slope angle as θ_{outlet} . Conversely, when going downhill (right), the nozzle has to be raised by t to avoid self-layer collision between the point on the right side of outlet (green dot) and the current layer. With the raising operation, no need to define any slope angle for the downhill case.

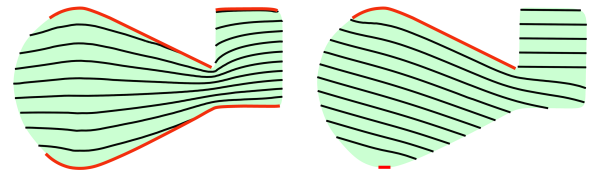


Fig. 7. An illustration that staircase minimization is not equivalent to continuity maximization. Left visualizes the CurviSlicer result with the target flat areas (initially attempt to flatten all areas under a specific slope angle, red segments). It could only flatten a part of the target flat areas to avoid violating layer thickness constraint. The result layers cannot produce OPP layers. Right shows the OPP layers and the specific target flat areas of our method. Note that different from CurviSlicer, the downward facing areas can also be taken as target flat areas thanks to the support structure constraint (subsection 3.1).

Finally, set the upper bound of the path slope angle as $\theta_{max} = \min(\theta_{nozzle}, \theta_{object}, \theta_{outlet})$ (30° in our test).

Support structure constraint. We decouple the fabrication of the intact model and support structures and add a membrane between them to facilitate removing operation of support structures. Such decoupling requires that the support structures be located on the ground and form a height field volume related to the printing orientation. The self-supported models are also valid. For a model with support structures on itself, the support structures have to be placed during the intact model fabrication. It's hard to place the membrane and remove the support structures in such a case. In addition, the external support structures may induce collapse of the part printed below while it has not been well solidified. We propose to decompose it into multiple patches and assemble them after fabrication (an example is shown in Figure 18).

3.2 One-Path-Patch (OPP)

Recall that we aim to optimize the continuity of ceramics printing of shell models by decomposing the minimal number of "one-path-patches" (OPPs). As formulated in Section 1, a manifold connected surface patch P is an OPP associated with a set of slicing elements (*segments* or *contours*) where all intersected elements come from different slicing layers under the fabrication constraints. Three types of OPP can be defined according to the slicing layers: (I) only flat layers; (II) only curved layers; (III) combination of I and II, named as I-OPP, II-OPP, and III-OPP for short, shown in Figure 4.

What geometric properties should an OPP hold? For type I, the OPP criterion is equivalent to its *monotonicity*¹, as (1,4) shown in Figure 4. As for type II, the intrinsic geometric properties of an OPP is hard to propose, where *monotonicity* becomes a sufficient and unnecessary condition. In Figure 4, (3,5,7) is an OPP but not *monotone*, and it demonstrates that a single OPP with curved layers could cover regions where multiple I-OPPs are applied.

To determine whether P is an II-OPP, one option can be extracting curved layers directly, then assess the two fabrication criteria.

¹A 2D polygon P is *monotone* with respect to a straight line L , if every line orthogonal to L , intersects P at most twice. A 3D manifold surface patch is *monotone* in direction L if all cross-sections orthogonal to L are single section [Toussaint 1985].

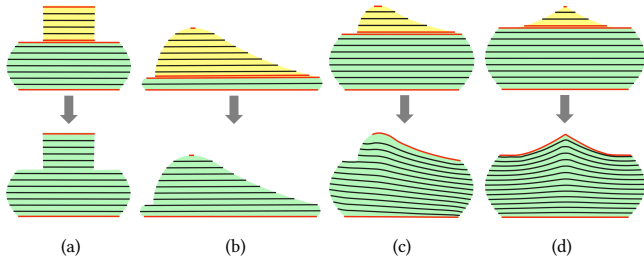
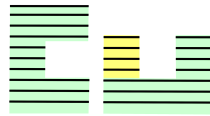


Fig. 8. Illustration of merging two OPPs by *stacking* operation (a)(b) and *curving* operation (c)(d). (a) and (b) cannot be merged via curved layers for violating the slope angle constraints and thickness constraint, respectively. The red segments indicate the top and bottom target flat areas.

CurviSlicer seems a perfect matching for this, which desires to flatten as many areas as possible to minimize staircases [Etienne et al. 2019]. However, staircase minimization is not always equivalent to continuity maximization, which is sensitive to the target flat areas taken as input of CurviSlicer, as shown in Figure 7. Two I/II-OPP can be merged to a single II-OPP (details in Section 3.3). For a whole shell model, a bottom-up OPP merging procedure is introduced to minimize the number of OPPs, during which process III-OPP (as (6,8,9) shown in Figure 4) are generated (Section 4.4).

To the best of our knowledge, OPP criterion had never been explored before. An OPP possesses three key properties to make it attractive as the elementary path generation element to maximize the continuity of ceramics printing for shell models:



- (1) The OPP criterion is defined with respect to a specific printing direction. An OPP in a printing direction (left) may not be an OPP with another direction (right), shown in the inset Figure.
- (2) Even with the same printing direction, valid slicing strategies of an OPP may not be unique. In Figure 4, (1) and (2) show two kinds of slicing layers where flat and curved slicing layers can be applied. Curved layers always produce fewer staircase which are associated with higher priority than flat layers.
- (3) Two OPPs can be merged to one single OPP. Two OPPs (A and B) can be merged via two operations, *stacking* and *curving*, as shown in Figure 8. *Stacking* indicates that 1) OPP A's bottom layer A_{bl} locates on the above neighboring layer of B's top layer B_{tl} ; 2) A_{bl} and B_{tl} can be connected by its two end points. *Curving* indicates the merging operation of Section 3.3. The two operations are used in Section 4.4 to minimize the number of OPPs.

3.3 Curving Operation

The input of this operation are two I/II-OPP (A and B) that can be originally merged via *stacking*. *Curving* operation aims to output the merged OPP (C) with its slicing layers. Suppose OPP A is above over B, as shown in Figure 8. Note that *curving* cannot be applied for two OPPs with only closed contours.

Our basic idea is to produce a modified version of CurviSlicer to extract curved layers for the merged OPP C. There are two key

questions: 1) how to determine the top/bottom target flat areas of C? 2) how to guarantee the fabrication constraints? We solve the first question by combining the top/bottom target flat areas of A and B. For the determined top/bottom target flat areas of C, detect the slope angle constraint. Then extract the in-between curved layers with our modified Curvislicer satisfying the fabrication constraints.

For an I-OPP, define the projection of its top (bottom) layer as its top (bottom) target flat areas (A_{tf} , A_{bf} , B_{tf} , B_{bf}). Starting traverse from the layer at the top layer of A, two oblique poly-lines can be obtained by connecting the two end points on both sides of each layer to the bottom layer. If both oblique lines violate the slope angle constraint, the two OPPs cannot be merged via curved layers. If not, we generate C's top target flat areas by combining 1) OPP A's top target flat areas (A_{tf}), 2) the difference result of B's top target flat areas and A's bottom target flat areas ($B_{tf} - A_{bf}$), 3) the oblique lines that meet the slope constraint; C's bottom target flat areas are taken from B's bottom target flat areas.

Next, we call CurviSlicer, specifying both top and bottom target flat areas. Without adopting the original version of CurviSlicer, we only use the flat term to determine whether the target area is flattened. In our case, it is unnecessary for the slope angle and thickness constraint detection. We leave the final toolpath smoothing in a post-optimization process. The merge is executable if the top and bottom target flat areas are successfully flattened without violating the fabrication constraints. We remove the most time-consuming smooth term used to make the generated curved layer smoother.

4 ACAP METHODOLOGY

This section describes our algorithm in more details. For clear exposition, we explain the methodology for open 2D patches with only *segments* in each layer. The extension to 3D will be discussed in the next section.

4.1 Orientation Assessment

Given the input model M , this step first extracts feasible printing orientations by uniformly sampling orientations over the Gaussian sphere then validating the *support structure constraint*. For these result orientations, determine an optimal one by evaluating the flatten area and support structure volume.

Support structure constraint validation. For each orientation, apply a similar method as [Hergel et al. 2019] to detect the support areas and validate the *support structure constraint*. First, slice the model and if a layer point requires support, project it downward. Suppose the first intersection point lies on the printing platform, add support points for the previous slicing layers below. If intersect with the model itself, it indicates violating the *support structure constraint*, shown in Figure 5(a). After traversing all layers, get a set of support points as the final support structures.

Optimal orientation determination. We propose an energy function by combining two quantifiable terms: $E_{ori} = \lambda * E_{flat} + (1 - \lambda) * E_{support}$, where E_{flat} and $E_{support}$ measure the low slope areas and the support volume, respectively. The optimal orientation is with the minimal energy ($\lambda = 0.8$ in our implementation). The details of E_{flat} and $E_{support}$ are elaborated in Appendix B.

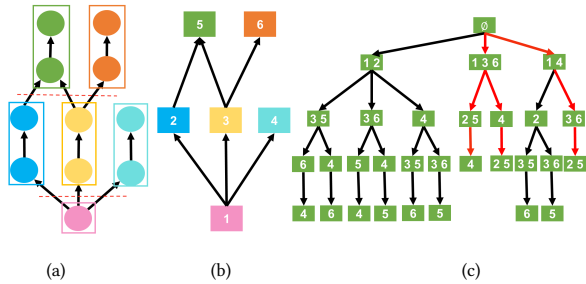


Fig. 9. (a): Dependency graph (G_{depend}), each node represents a sliced element. (b): Nodes are merged into initial OPP graph (G_{init}). (c): The path cover solution space of G_{init} , every path from root to leaf is a path cover solution. Three red paths are optimal with the minimal number of OPPs. Note that three paths produce two unique OPP graphs shown in the inset Figure of subsection 4.3.

4.2 Building Dependency Graph

As a preparatory step of the following OPP merging process, we uniformly slice the model with flat planers by t (1.0mm in our experiments) vertical to the printing orientation and build a dependency graph G_{depend} , where each node represents a sliced element (*segment*), and each edge represents a dependency relationship between nodes, shown in Figure 5(b). If node N_1 has a directed edge pointing to N_2 , N_2 can be printed only after N_1 , call it " N_2 depends on N_1 ". A node can be printed only if all nodes it depends on have already been printed.

4.3 OPP Merging through Flat Layers

This section aims at maximal continuity provided by flat slicing, that is, merging the flat sliced elements of G_{depend} to a minimal number of I-OPPs. Each sliced element can be seen as an I-OPP, which can be merged by *stacking* operation (subsection 3.2). The merged I-OPPs should keep the dependency relationships formulated in G_{depend} . Such merging process is indeed a PC-MPC problem, to find a path cover for G_{depend} having the fewest paths considering the dependency relationships (as the precedence constraint of PC-MPC).

To make the NP-hard problem tractable, we propose two key steps for the merging process: 1) merge the nodes of G_{depend} that must appear on the same path in any minimum path cover in advance, then build an initial OPP graph G_{init} to reduce the size of G_{depend} . 2) merge the nodes of G_{init} further by solving the PC-MPC problem of G_{init} . Rather than running an approximation algorithm, we propose a searching-based method with a pruning strategy to explore the possible solutions.

Initial OPP graph. To build a simplified graph G_{init} from G_{depend} , we traverse all nodes of G_{depend} , if there are two or more edges pointing to the same node or starting from the same node, delete these edges (dashed red lines in Figure 9(a)). Then compute the connected components, each component acts as a node of G_{init} , which can be seen as a merged larger I-OPP by *stacking*. Such merging process maintains the optimality of the PC-MPC problem, that is, the sub-nodes of a G_{init} node must belong to a single path of the

optimal solution of the PC-MPC problem². The dependencies of G_{init} are inherited from G_{depend} . As shown in Figure 9(a)(b), the scale of the graph is significantly reduced.

Searching based PC-MPC algorithm. OPP nodes of G_{init} can further merge via *stacking*, as shown (1,2), (1,3,6), (3,5) in Figure 9(b). A path cover of G_{init} presents a feasible merging solution. As $\{(1,2), (3,5), (4), (6)\}$, it produces four I-OPPs, and the dependency relationships are preserved, that is, (3,5) depends on (1,2), (6) on (3,5) and (4) on (1,2). Such path cover solution can be obtained from a specific depth-first tree traversal procedure of G_{init} starting from the root node. A connected traversal path is taken as a merged I-OPP. Different from a general DFS, it may not explore as far as possible to the leaf node before backtracking. The traversal has to stop while a node's dependent nodes have not been explored, such as (1,2,5) is not valid that (3) is not explored.

For merging G_{init} to the minimal number of I-OPPs, a straightforward but time-consuming method is to traverse G_{init} by attempting all possible branches. We propose two key techniques to speed up such exploration by pruning the search space. First, use a greedy strategy that each traversal path would explore as deep as possible, as (1,3) will continue to include (6) in Figure 9(b). We proved that the calculated solution is not optimal without this strategy³. Second, apply the branch and bound technique during the exploration.

See Figure 9(c), a path cover solution space represented with a tree structure is built along with the exploration procedure, where the root node is a blank node, the non-root nodes are merged I-OPPs, the directed edges encode the printing orders of I-OPPs, every path from the root node to the leaf node indicates an path cover solution. Starting from the root node of G_{init} , we apply a beam search procedure to explore the solution space, where the beam search width is set to $W = 10^4$ in our implementation, and for every candidate path, the priority score is determined by the number of G_{init} 's nodes it contains, it implies that when picking a path into current path cover at a time, we tend to pick the one contains G_{init} 's nodes as many as possible. The pseudo-code is presented in Appendix C.

The results of the proposed method can be not unique, as the two optimal solutions in Figure 9(c). See the inset Figure, each path cover solution is related to an OPP graph G_{OPP} where each node is the merged nodes, and edges indicate dependency relationships. Each node of G_{OPP} is comprised of a sequence of I/II-OPPs (denoted as *sub-OPPs*), where the sequence edges indicate the printing order. Take the inset Figure (left) as an example; the blue node's sub-OPPs are (1,3,6). For most of our test results, the proposed method can compute all the optimal solutions, since we have searched for all possible solutions that could be optimal (a

²This can be proved by contradiction. If two adjacent sub-nodes belong to two paths of an optimal solution, they must be terminal nodes of the paths. Obviously, the two paths can be connected further, which indicates the current path cover solution is not optimal.

³In the traversal path process, if terminating the path when a node can be added, the node must be the starting point of another path. In the same way as the last proof, the number of paths of path cover, in this case, is at least 1 more than our strategy, so it is not optimal.

solution not in our solution space is not optimal). However, for some complex models, such as *TPMS* model, we cannot make guarantee that output path cover is globally optimal, since the solution space searched by the width of beam search we set is not enough to contain all possible optimal solutions.

4.4 OPP Merging through Curved Layers

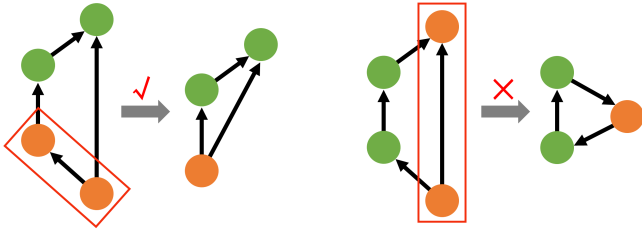


Fig. 10. Illustration of printing dependency deadlock, the orange nodes represent the pair of selected nodes in DAG. Left: Only one path exists between the two nodes, there will be no deadlock loops generated after merging. Right: with two or more paths existing between the two nodes, deadlock loops be produced after merging, that is, the nodes are inter-dependent and cannot be printed, thus prohibiting merging.

Up to now, we obtained a set of unique G_{OPP} composed of only I-OPPs. For each G_{OPP} , this section aims to further merge its OPP nodes via *curving*. The basic idea is to apply the *curving* operation to these sub-OPPs of two OPPs, which may make the two OPPs mergeable to one OPP via *stacking*. We propose a pair-wise based merging procedure for each G_{OPP} (**outer loop**). During each iteration, try to merge two OPP nodes of G_{OPP} which recursively calls a similar pair-wise based merging procedure (**inner loop**). That is, we use the same graph merging process for both G_{OPP} merging (outer loop) and two OPPs merging (inner loop). II-OPPs and III-OPPs would be generated during the merging process.

For a general directed acyclic graph (DAG), a pair-wise merging procedure can be applied. For each iteration, randomly select an edge and try to merge the two related nodes with specific merging criteria to check whether they can be merged or not. If yes, update the graph by 1) merging a pair of nodes to one node, 2) erasing the edge of the two nodes and 3) pointing other related edges of the two nodes to the merged node. The terminal condition is that no pairs of nodes can be merged.

In our case, the edges of DAG indicate dependency relationships of OPPs. While merging a pair of nodes, one necessary criterion is to guarantee there are no multiple paths between the two nodes, since it will result in a deadlock of dependency after merging, shown in Figure 10 (right). For the outer loop, since G_{OPP} is a DAG, the pair-wise merging strategy can be applied to G_{OPP} directly (Figure 11 (a~c)).

As for the inner loop, a DAG can be formulated from the two candidate merging OPP nodes: 1) take their sequences of sub-OPPs where each sub-OPP is a node and maintain the dependency edges of these sub-OPPs; 2) add back the associated dependency edges between the two sequences from G_{init} . While applying the pair-wise merging strategy to the result DAG (Figure 11 (d~g)), we only select

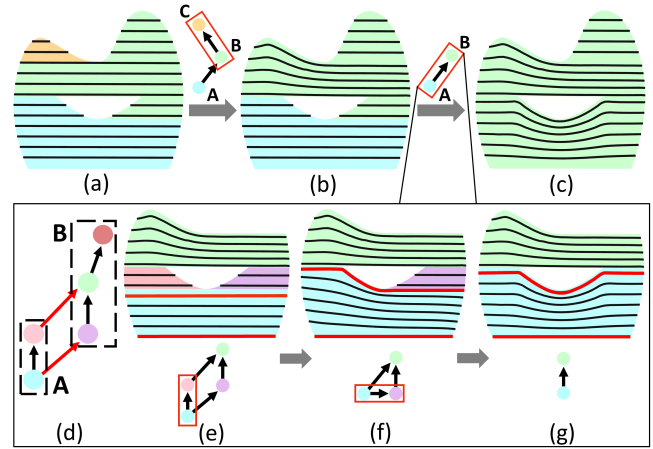


Fig. 11. A mesh is decomposed to three I-OPPs, corresponding to G_{OPP} with three nodes (a). In the outer loop (in G_{OPP}), iteratively merge nodes pair by pair to one node, that is, one III-OPP finally (c). (d) ~ (g) shows the merging process in the inner loop of (b) to (c), A and B show two sequences of sub-OPPs in (d), and only the four nodes connected by red edges in (d) are selected to merge, *curving* operation is used for the merging in inner loop. Since two OPPs of (g) accept *stacking* into one OPP, node A and B can successfully merge in the outer loop.

edges that benefit merging the two sequences to a single sequence. Specifically, we label the nodes which have edges across the two sub-OPP sequences (two red edges shown in (d)), then select edges over such labeled nodes. For each pair of nodes, call *curving* operation to merge them (subsection 3.3). The pseudo-code is presented in Appendix C.

It is worth mentioning that we apply the *curving* operation as much as possible for merging a pair of nodes in both inner and outer loops, considering curved layer helps improve staircase effect. As shown in Figure 11(f), although these OPPs can *stacking* into one OPP, we perform *curving* to (g).

For different G_{OPP} of input, the final number of nodes after merging may be different. We randomly select one G_{OPP} with the least number of nodes since we only consider the OPP number criterion. Different G_{OPP} and order of merging OPPs by *curving* may result curved layers with different distributions, in other words, different sub-OPP of the final III-OPP, as shown in the inset Figure. Similarly, since the order of selecting nodes in two levels is random, we cannot guarantee the global optimal solution. Figure 21 shows an example, and more details will be discussed in Section 7.

4.5 Toolpath Generation

With the bottom-up merging OPP process, we get an optimal OPP decomposition. This section works on path planning for each OPP by converting OPP slicing layers to continuous toolpath and generating

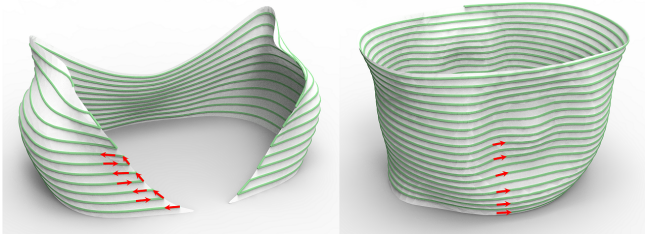
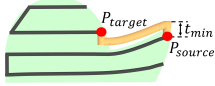


Fig. 12. Zig-zag connecting path for *segments* (left) and Spiral connecting path for *contours* (right).

transfer moves between OPPs. Note that we remove the most time-consuming smooth term of CurviSilcer while applying the *curving* operation during OPP merging (subsection 3.3). Here we add it back and rebuild the smoother curving layers of related OPPs for the toolpath planning. Then connect inter-layer to a single path for each OPP and determine the fabrication order of these OPP paths.

Inter-layer connection path. Since there are only *segments* in 2D models, they can be connected using zig-zag pattern. We set a Euclidean distance threshold $D = 10mm$ to determine whether two terminal points of two neighboring layers can be connected directly with a straight segment. If not (exceeds D), add a few extra paths. See the inset Figure, call the current terminal point in the current layer P_{source} , and the terminal point needs to be connected in the next layer P_{target} . Print along the current printed layer with t_{min} layer thickness from P_{source} to the position closest to P_{target} , and then print along straight line to P_{target} (the orange path in inset Figure). The post path optimization in Section 5 will improve the spatial distribution of the generated extra path.



OPPs sequence. With the known dependency relationships of these OPP paths, we apply a greedy method as subsection 4.3 to produce a feasible fabrication order. Then, we plan travel moves between OPP paths by withdrawing the nozzle to a safe distance above the printed objects to avoid possible collisions (see Figure 1). Finally, a G-code file is generated to transfer the toolpath to the printer.

5 EXTENSION TO 3D

Extending our algorithm from 2D to 3D does not require extra effort for most steps, except to deal with *contour* in the G_{init} construction step and extend the toolpath generation step for the 3D case. In this section, we describe the extension of these steps in detail.

Initial OPP graph. For 3D cases with contours, we first build a G_{init} with the method of subsection 4.3. If an OPP node of G_{init} has both segments and contours, divide it into pure segment nodes and pure contour nodes. Such classification is conducive to the next step of merging via *curving*, which only allows the input of two OPPs composed of *segments*, or one OPP composed entirely of *segments*, and the other entirely of *contours*.

Contour spiralization. As mentioned, *segments* of an OPP would be connected following a Zig-zag pattern. For the OPP's *contours*,

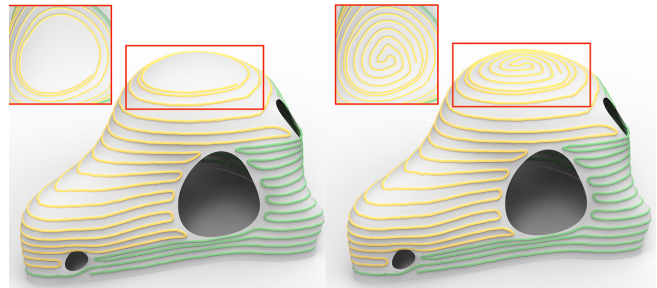


Fig. 13. Under-fills appears at the top of the model because of inadequate slicing in low-slope region (left). Filling the area with connected Fermat spirals (right), the top of model is printed completely.

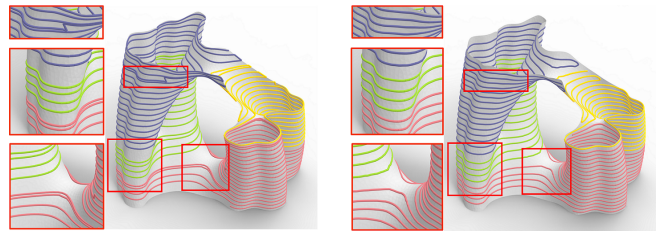


Fig. 14. Effectiveness of global path optimization. Left: without global path optimization, some paths are too close or too far. Right: global path optimization leads to uniform path.

we connect them by Spiral path, shown in Figure 12. The basic idea is to extract an interpolation curve between each two adjacent contours, then connect these curves to a single spiral. First, determine an entry point for each contour where the key consideration is to minimize the total distance between adjacent entry points. Second, for each two adjacent contours, interpolate all sampling points starting from the entry points:

$$P_i = w \cdot P_a + (1 - w) \cdot P_b, \quad w = S_{current} / S_{total}$$

where P_b is a sampling point of the below contour, P_a is the nearest point to P_b of the above contour, S_{total} is total length of the below contour, $S_{current}$ is the geodesic distance that P_b moves from the entry point along the below contour, P_i is the interpolation point.

Filling the low slope area. While slicing, inadequate layers over low-slope regions inevitably result in under-fills, shown in Figure 13 (left). Such under-fills of small areas can be removed by a post path optimization process (see Figure 14 left bottom). For larger under-fill areas, we propose to fill them with connected Fermat spirals [Zhao et al. 2016]. In our implementation, we set a threshold of 20° to detect the flat areas. Figure 13 (right) shows the filling path over the original 3D surface.

Toolpath optimization. Since we generate toolpath for each OPP separately, the adjacent paths may be too close or too far from each other (left center of Figure 14 (left)). Some inter-layer connection paths (subsection 4.5) and the filling paths of low slope areas (left bottom of Figure 14 (left)) may be not uniformly distributed (left top of Figure 14 (left)). To eliminate these problems, we use a similar

method as [Zhao et al. 2018] to optimize the final toolpath. Different from the original method, our input is not a single path but multiple continuous paths. Figure 14 shows a result before and after optimization.

6 RESULTS AND DISCUSSION

This section shows OPP decomposition results on shell models with varying geometric complexity, printed results, and comparisons with the Ultimaker Cura software.

6.1 Implementation and parameters

Our algorithm is implemented in C++, running on a PC with an Intel Core i7-9700 CPU @ 3.0GHz and 32GB memory. For the printing experiment, we use a 3-axis ceramic printer *Eazao Mega 5* based on DIW technique with $470mm \times 370mm \times 390mm$ printing platform (Figure 17-left). This machine relies on an air pump to extrude clay. We use a slender, $90.0mm$ long nozzle with outlet radius as $2.6mm$ (Figure 17-right), nozzle movement speed as $25.0mm/s$. The printing layer width is $3mm \sim 6mm$. The slope angle constraint according to the formulation in Section 3.1 is 30° . We set the flat layer thickness to $1.0mm$, producing the best surface quality in our experiments, and also use it as the slicing layer thickness to slice models and generate G_{depend} . During the algorithm, we set $\lambda = 0.8$ for orientation assessment (section 4.1), the beam search width $W = 10^4$ in searching based PC-MPC algorithm (section 4.3), and the distance threshold $D = 10mm$ in connecting layers (section 4.5).

6.2 Printed models

Model	H	#OF	#OO	#OC	t-Ours	t-Cura
 Julia vase	81	9	4	195	17min43s	34min18s
 Grail	120	2	1	113	20min08s	26min42s
 Crown	38	6	2	76	8min16s	12min28s
 TPMS	95	18	18	491	37min17s	58min30s
 Shoe	52	2	1	N/A	20min42s	N/A
 Ocean	79	4	2	N/A	59min32s	N/A
 Mask	54	6	2	N/A	8min38s	N/A

Table 1. Statistics of the results. H is the model height (mm). #OF is the number of OPPs that our method uses only flat layers. #OO is the final number of OPPs using both flat and curved layers. #OC is the number of OPPs for Cura. t-Ours and t-Cura indicate the printing time of our method and Cura, respectively.

Figure 1 shows the printed *Julia vase* model, with our method and Cura. There are 4 separated columns in the middle part of the model, and thus Cura failed to spiralize the multiple-contour layers, producing 195 disconnected printing toolpaths. Our method decomposes the model into 4 OPPs and generates the ACAP toolpath along both flat and curved slicing layers, thus achieving superior printing quality and reducing the printing time by almost half.

Figure 15 and 16 show more results in two groups, including OPP decomposition, printing path, and printed models. Refer to Table 1 for the statistics of these models. We list the resulted number of

OPPs (#OO) after the bottom-up merging algorithm as well as the intermediate result, i.e., the number of OPPs after merging through flat layers (#OF), to illustrate the effectiveness of *stacking* and *curving* operations.

In Figure 15, the three models are self-supported. We choose the surface mode and enable spiralize outer contour in the settings of Cura, and perform fabrication with the same parameters for both methods. It shows that our method outperforms Cura significantly for shell models containing multiple *contours* or *segments* in both surface quality and fabrication efficiency. See the *Grail* model printed with Cura, a large number of transfer moves induce artifacts in surface quality. Moreover, such transfer moves increase the shearing forces on the printed part and may cause the collapse of the whole model. In contrast, the ACAP toolpath for this model is fully continuous and thus avoids these problems.

In Figure 16, we show the shell models with support structures and after removing them. Note that Cura cannot generate support for shell surfaces and is thus invalid for these models. In the experiments, we print support structures in advance and then add a membrane before printing the intact model.

Model	Ori_Sel	OPP_Mrg	Path_Opt
 Julia vase	8min6s	8min40s	5min26s
 Grail	3min17s	3s	7min18s
 Crown	2min25s	7min13s	2min24s
 TPMS	13min42s	5s	7min35s
 Shoe	2min22s	3s	53s
 Ocean	5min12s	19s	1min34s
 Mask	7min55s	9min37s	4min2s

Table 2. Statistics of the algorithm time cost. It consists of three parts: orientation assessment (Ori_Sel), OPP merging (OPP_Mrg) and toolpath optimization (Path_Opt).

6.3 Timings

The major computational cost of our framework includes orientation assessment, OPP merging, and toolpath optimization. Table 2 shows the running time statistics. The cost of orientation selection mainly depends on the mesh size, as both flatness and support volume are computed per facet. The OPP merging cost varies greatly, related to the search complexity of the PC-MPC problem and the number of OPPs for *curving*. See *Grail*, *Shoe*, and *Ocean* model, there are few optimal solutions of PC-MPC, making the running time short. For *TPMS* model, its G_{init} is large and thus requires relatively long time in the PC-MPC search; however, no OPP allows *curving* operation for violating the slope constraint, the running time of OPP merging is also short. For toolpath optimization, the main factor of running time is the path length.

6.4 Discussion

In general, we can see that our framework outperforms the existing method in terms of high printing quality, short printing time, and easy-to-remove support. Now we discuss some derivative results.



Fig. 15. Some results of self-supported models. The OPP decomposition, toolpath and printed results by our method and Cura (rightmost column) are shown respectively.

Decompose and Assemble. It is worth mentioning that although we have a hard support structure constraint (subsection 3.1), we can decompose the model when no feasible orientation exists. As shown in Figure 18, we manually decompose the kitten into three patches like [Mitropoulou et al. 2020] did, run our framework for each patch separately, and finally assemble them. We remark that different degrees of shrinkage may leave noticeable seam lines between parts after hardening. We regard this as an interesting but orthogonal problem for this paper.

Geometric texture. Our method generates G-code files containing all path information. It can be directly used as the input of [Yan et al. 2021]’s framework to embed with geometric textures without violating the toolpath continuity. Each OPP can be used as an independent unit to embed different textures, producing some interesting results (see Figure 19).

7 CONCLUSION, LIMITATION, AND FUTURE WORK

In extrusion-based ceramic 3D printing, path continuity significantly impacts the surface quality and printing time, especially for shell models. We put forward the original concept of OPP to quantify path continuity and propose a method to decompose the given shell model into as few OPPs as possible, considering manufacturing constraints on a standard three-axis printer platform. Besides, we decouple the shell model and support structure during printing,

making it easy to remove the support structure. We demonstrated our methods in various models, and the results are superior to existing methods in surface finish and printing time.

Limitation and Future work. The first limitation is we cannot ensure the number of OPPs is optimal. When choosing two OPPs *curving*, different orders may lead to different results. Figure 21 is an extreme example. The middle green OPP of (a) meets the layer thickness constraint when *curving* with only the upper or lower OPP. However, if attempts to merge the upper and lower OPP together, the constraint will be violated. The two different orders of OPP *curving* ((b) and (c)) result in a different number of final OPPs.

On the manufacturing side, when printing curved layers at downhill parts, a groove will appear due to the over-squeeze of the nozzle; the layer thickness will be thinner in the middle and thicker on both sides. Since the zig-zag curved path goes uphill and downhill alternately, clay at uphill parts will be stuck in the groove. So the layer thickness will be thicker downhill and thinner uphill from the side view, as shown in Figure 20. Physical simulations of the material behavior during fabrication would help conquer this problem.

Considering the stability during ceramic printing for that the extruding clay can not be solidification immediately to support above layers, [Xing et al. 2021] proposed to locally enhance the structural stability by shell thickening for self-supported models.



Fig. 16. Some results of models with support. The OPP decomposition, toolpath and printed results by our method are shown respectively.



Fig. 17. The three-axis printer *Ezao Mega 5* for experiments (left) with a slender nozzle (right).

While it's not straightforward to extend their method to shell models with support structures.

Last but not least, the ACAP pipeline ignores a potential collision problem. If the height difference between the printed objects and the next OPP is greater than the nozzle, the printer carriage may collide with the printed objects while travel moves. To alleviate this



Fig. 18. For the kitten model not satisfied the support constraint, we manually decompose it into three patches satisfying the support constraint (left), separately print them using our ACAP toolpaths (middle), and assemble them afterwards (right).

issue, our printer uses a slender nozzle to make the carriage far from the printed objects.

In the future, comprehensive consideration of the shell model's physical properties is meaningful, demanding force analysis on the



Fig. 19. Julia vase model is decomposed into four OPPs, embedded into different textures.



Fig. 20. The layer thickness is thicker downhill and thinner uphill from the side view in Zig-zag curved path (left), it's due to the groove generated by the over-squeeze of nozzle at downhill parts (right).

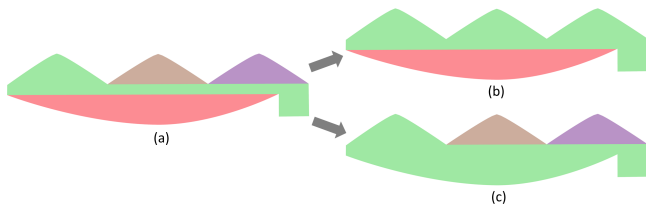


Fig. 21. Four I-OPPs can be decomposed by solving PC-MPC (a). If give priority to *curving* green, brown and purple OPPs, they can merge in sequence and finally merge into two OPPs (b). However, if firstly *curving* green and red OPPs, the remaining OPPs cannot merge due to the layer thickness constraint, and the final number of OPPs is three (c).

printed model and optimizing geometric structure. One of the most intuitive methods is to adjust the wall thickness by controlling the amount of extrusion, but some areas may need multiple layers to enhance the physical properties, and maintaining the continuity of path at the same time may be a problem worth exploring.

On the other hand, considering our support structure constraint, an automated pre-decomposition algorithm will be focused on. How to balance the number of decomposed patches and path continuity may be a challenging problem.

Finally, extending our OPP definition and decomposition methods to solid models or other printing techniques can be interesting and valuable. One possibility is to generalize the OPP decomposition from surface to that in volume. Another problem worth exploring is extending them to multi-axis printers such that the slope angle

constraint can be ignored, and the path has more freedom. We believe the research direction owns great potential.

REFERENCES

- Robert J.A. Allen and Richard S. Trask. 2015. An experimental demonstration of effective Curved Layer Fused Filament Fabrication utilising a parallel deposition robot. *Additive Manufacturing* 8 (oct 2015), 78–87. <https://doi.org/10.1016/j.addma.2015.09.001>
- Ana Anton, Angela Yoo, Patrick Bedarf, Lex Reiter, Timothy Wangler, and Benjamin Dillenburger. 2019. Vertical Modulations. Computational design for concrete 3D printed columns. In *ACADIA 19: Ubiquity and Autonomy. Proceedings of the 39th Annual Conference of the Association for Computer Aided Design in Architecture*, Kory Bieg, Danelle Briscoe, and Clay Odom (Eds.). Association for Computer Aided Design in Architecture (ACADIA), s.l., 596 – 605.
- Prahar M. Bhatt, Rishi K. Malhan, Pradeep Rajendran, and Satyandra K. Gupta. 2020. Building free-form thin shell parts using supportless extrusion-based additive manufacturing. *Additive Manufacturing* 32 (mar 2020), 101003. <https://doi.org/10.1016/j.addma.2019.101003>
- Shajay Bhooshan, Tom Van Mele, and Philippe Block. 2020. Morph & Slerp: Shape description for 3D printing of concrete. *Symposium on Computational Fabrication* (nov 2020). <https://doi.org/10.1145/3424630.3425413>
- B.Huang and S.Singamneni. 2012. Alternate slicing and deposition strategies for fused deposition modelling of light curved parts. *Journal of achievements in materials and manufacturing engineering* 55 (2012), 511–517.
- Joris Burger, Ena Lloret-Fritsch, Fabio Scotto, Thibault Demoulin, Lukas Gebhard, Jaime Mata-Falcón, Fabio Gramazio, Matthias Kohler, and Robert J. Flatt. 2020. Eggshell: Ultra-Thin Three-Dimensional Printed Formwork for Concrete Structures. *3D Printing and Additive Manufacturing* 7, 2 (apr 2020), 48–59. <https://doi.org/10.1089/3dp.2019.0197>
- Debapriya Chakraborty, B. Aneesh Reddy, and A. Roy Choudhury. 2008. Extruder path generation for Curved Layer Fused Deposition Modeling. *Computer-Aided Design* 40, 1 (feb 2008), 235–243. <https://doi.org/10.1016/j.cad.2007.10.014>
- Shareen S.L. Chan, Ryan M. Pennings, Lewis Edwards, and George V. Franks. 2020. 3D printing of clay for decorative architectural applications: Effect of solids volume fraction on rheology and printability. *Additive Manufacturing* 35 (oct 2020). <https://doi.org/10.1016/j.addma.2020.101335>
- Lufeng Chen, Man-Fai Chung, Yaobin Tian, Ajay Joneja, and Kai Tang. 2019a. Variable-depth curved layer fused deposition modeling of thin-shells. *Robotics and Computer-Integrated Manufacturing* 57 (jun 2019), 422–434. <https://doi.org/10.1016/j.rcim.2018.12.016>
- Zhangwei Chen, Ziyong Li, Junjie Li, Chengbo Liu, Changshi Lao, Yuelong Fu, Changyong Liu, Yang Li, Pei Wang, and Yi He. 2019b. 3D printing of ceramics: A review. *Journal of the European Ceramic Society* 39, 4 (apr 2019), 661–687. <https://doi.org/10.1016/j.jeurceramsoc.2018.11.013>
- Chengkai Dai, Charlie C. L. Wang, Chenming Wu, Sylvain Lefebvre, Guoxin Fang, and Yong-Jin Liu. 2018. Support-free volume printing by multi-axis motion. *ACM Transactions on Graphics* 37, 4 (aug 2018), 1–14. <https://doi.org/10.1145/3197517.3201342>
- Jimmy Etienne, Nicolas Ray, Daniele Panozzo, Samuel Hornus, Charlie C. L. Wang, Jonàs Martínez, Sara McMains, Marc Alexa, Brian Wyvill, and Sylvain Lefebvre. 2019. CurviSlicer: Slightly curved slicing for 3-axis printers. *ACM Transactions on Graphics* 38, 4 (jul 2019), 1–11. <https://doi.org/10.1145/3306346.3323022>
- Ben Ezair, Saul Fuhrmann, and Gershon Elber. 2018. Volumetric covering print-paths for additive manufacturing of 3D models. *Computer-Aided Design* 100 (jul 2018), 1–13. <https://doi.org/10.1016/j.cad.2018.02.006>
- Guoxin Fang, Tianyu Zhang, Sikai Zhong, Xiangjia Chen, Zichun Zhong, and Charlie C. L. Wang. 2020. Reinforced FDM: multi-axis filament alignment with controlled anisotropic strength. *ACM Transactions on Graphics* 39, 6 (nov 2020), 1–15. <https://doi.org/10.1145/3414685.3417834>
- Jean Hergel, Kevin Hinz, Sylvain Lefebvre, and Bernhard Thomaszewski. 2019. Extrusion-based ceramics printing with strictly-continuous deposition. *ACM Transactions on Graphics* 38, 6 (nov 2019), 1–11. <https://doi.org/10.1145/3355089.3356509>
- Philipp Herholz, Wojciech Matusik, and Marc Alexa. 2015. Approximating free-form geometry with height fields for manufacturing. *Computer Graphics Forum* 34, 2 (2015), 293–251. <https://doi.org/10.1111/cgf.12556>
- Kristian Hildebrand, Bernd Bickel, and Marc Alexa. 2013. Orthogonal slicing for additive manufacturing. *Computers & Graphics* 37, 6 (2013), 669–675. <https://doi.org/10.1016/j.cag.2013.05.011>
- Samuel Hornus, Tim Kuipers, Olivier Devillers, Monique Teillaud, Jonàs Martínez, Marc Glisse, Sylvain Lazard, and Sylvain Lefebvre. 2020. Variable-width contouring for additive manufacturing. *ACM Transactions on Graphics* 39, 4 (jul 2020). <https://doi.org/10.1145/3386569.3392448>
- Ruizhen Hu, Honghua Li, Hao Zhang, and Daniel Cohen-Or. 2014. Approximate Pyramidal Shape Decomposition Ruizhen. *ACM Transactions on Graphics* 33, 213 (nov 2014), 1–12. <https://doi.org/10.1145/2661229.2661244>

- Mikio Kubo and Hiroshi Kasugai. 1991. The precedence constrained traveling salesman problem. *Journal of the Operations Research Society of Japan* 34, 2 (1991), 152–172. <https://doi.org/10.15807/jorsj.34.152>
- Samuel Lensgraf and Ramgopal R. Mettu. 2016. Beyond layers: A 3D-aware toolpath algorithm for fused filament fabrication. In *2016 IEEE International Conference on Robotics and Automation (ICRA)*. IEEE. <https://doi.org/10.1109/icra.2016.7487546>
- Samuel Lensgraf and Ramgopal R. Mettu. 2017. An improved toolpath generation algorithm for fused filament fabrication. In *2017 IEEE International Conference on Robotics and Automation (ICRA)*. IEEE. <https://doi.org/10.1109/icra.2017.7989141>
- Samuel Lensgraf and Ramgopal R. Mettu. 2018. Incorporating Kinematic Properties into Fused Deposition Toolpath Optimization. In *2018 IEEE/RSJ International Conference on Intelligent Robots and Systems (IROS)*. IEEE. <https://doi.org/10.1109/iros.2018.8594398>
- Thomas Llewellyn-Jones, Robert Allen, and Richard Trask. 2016. Curved Layer Fused Filament Fabrication Using Automated Toolpath Generation. *3D Printing and Additive Manufacturing* 3, 4 (dec 2016), 236–243. <https://doi.org/10.1089/3dp.2016.0033>
- Linjie Luo, Ilya Baran, Szymon Rusinkiewicz, and Wojciech Matusik. 2012. Chopper: Partitioning Models into 3D-Printable Parts. *ACM Transactions on Graphics* 31, 129 (nov 2012), 1–9. <https://doi.org/10.1145/2366145.2366148>
- Ali Mahdavi-Amiri, Fenggen Yu, Haisen Zhao, Adriana Schulz, and Hao Zhang. 2020. VDAC: volume decompose-and-carve for subtractive manufacturing. *ACM Transactions on Graphics (TOG)* 39, 6 (2020), 1–15.
- Ioanna Mitropoulou, Mathias Bernhard, and Benjamin Dillenburger. 2020. Print Paths Key-framing. In *Symposium on Computational Fabrication*. ACM. <https://doi.org/10.1145/3424630.3425408>
- Alessandro Muntoni, Marco Livesu, Riccardo Scateni, Alla Sheffer, and Daniele Panozzo. 2018. Axis-Aligned Height-Field Block Decomposition of 3D Shapes. *ACM Transactions on Graphics* 37, 5 (nov 2018), 1–15. <https://doi.org/10.1145/3204458>
- Edisson Ordoñez, Jhon M. Gallego, and Henry A. Colorado. 2019. 3D printing via the direct ink writing technique of ceramic pastes from typical formulations used in traditional ceramics industry. *Applied Clay Science* 182 (dec 2019). <https://doi.org/10.1016/j.clay.2019.105285>
- Erwin Peng, Danwei Zhang, and Jun Ding. 2018. Ceramic Robocasting: Recent Achievements, Potential, and Future Developments. *ADVANCED MATERIALS* (oct 2018). <https://doi.org/10.1002/adma.201802404>
- Carlos F. Revelo and Henry A. Colorado. 2018. 3D printing of kaolinite clay ceramics using the Direct Ink Writing (DIW) technique. *Ceramics International* 44 (apr 2018), 5673–5682. <https://doi.org/10.1016/j.ceramint.2017.12.219>
- Godfried T Toussaint. 1985. Movable separability of sets. *Machine Intelligence and Pattern Recognition* 2 (1985), 335–375.
- J. Vanek, J. A. Garcia Galicia, B. Benes, R. Mech, N. Carr, O.Stava, and G.S. Miller. 2014. PackMerger: A 3D Print Volume Optimizer. *Computer Graphics Forum* 33, 6 (sep 2014), 322–332. <https://doi.org/10.1111/cgf.12353>
- Xiangzhi Wei, Siqi Qiu, Lin Zhu, Ruiliang Feng, Yaobin Tian, Juntong Xi, and Youyi Zheng. 2018. Toward Support-Free 3D Printing: A Skeletal Approach for Partitioning Models. *IEEE TRANSACTIONS ON VISUALIZATION AND COMPUTER GRAPHICS* 24, 10 (oct 2018), 2799–2812. <https://doi.org/10.1109/TVCG.2017.2767047>
- Chenming Wu, Chengkai Dai, Guoxin Fang, Yong-Jin Liu, and Charlie C.L. Wang. 2017. RoboFDM: A robotic system for support-free fabrication using FDM. In *2017 IEEE International Conference on Robotics and Automation (ICRA)*. IEEE. <https://doi.org/10.1109/icra.2017.7989140>
- Chenming Wu, Chengkai Dai, Guoxin Fang, Yong-Jin Liu, and Charlie C. L. Wang. 2020. General Support-Effective Decomposition for Multi-Directional 3-D Printing. *IEEE Transactions on Automation Science and Engineering* 17, 2 (apr 2020), 599–610. <https://doi.org/10.1109/tase.2019.2938219>
- Lingwei Xia, Sen Lin, and Guowei Ma. 2020. Stress-based tool-path planning methodology for fused filament fabrication. *Additive Manufacturing* 32 (mar 2020), 101020. <https://doi.org/10.1016/j.addma.2019.101020>
- Yu Xing, Yu Zhou, XinYan, Haisen Zhao, Wenqiang Liu, Jingbo Jiang, and Lin Lu. 2021. Shell thickening for extrusion-based ceramics printing. *Computers & Graphics* 97 (jun 2021), 160–169. <https://doi.org/10.1016/j.cag.2021.04.031>
- Ke Xu, Yingguang Li, Lufeng Chen, and Kai Tang. 2019. Curved layer based process planning for multi-axis volume printing of freeform parts. *Computer-Aided Design* 114 (sep 2019), 51–63. <https://doi.org/10.1016/j.cad.2019.05.007>
- Xin Yan, Lin Lu, Andrei Sharf, Xing Yu, and Yulu Sun. 2021. Man-made by Computer: On-the-Fly Fine Texture 3D Printing. *Symposium on Computational Fabrication* (oct 2021). <https://doi.org/10.1145/3485114.3485119>
- Chanyeol Yoo, Samuel Lensgraf, Robert Fitch, Lee M. Clemon, and Ramgopal Mettu. 2020. Toward Optimal FDM Toolpath Planning with Monte Carlo Tree Search. In *2020 IEEE International Conference on Robotics and Automation (ICRA)*. IEEE. <https://doi.org/10.1109/icra40945.2020.9196945>
- Xiaoya Zhai and Falai Chen. 2019. Path Planning of a Type of Porous Structures for Additive Manufacturing. *Computer-Aided Design* 115 (oct 2019), 218–230. <https://doi.org/10.1016/j.cad.2019.06.002>
- Haisen Zhao, Fanglin Gu, Qi-Xing Huang, Jorge Garcia, Yong Chen, Changhe Tu, Bedrich Benes, Hao Zhang, Daniel Cohen-Or, and Baoquan Chen. 2016. Connected format spirals for layered fabrication. *ACM Transactions on Graphics* 35, 4 (jul 2016), 1–10. <https://doi.org/10.1145/2897824.2925958>
- Haisen Zhao, Hao Zhang, Shiqing Xin, Yuanmin Deng, Changhe Tu, Wenping Wang, Daniel Cohen-Or, and Baoquan Chen. 2018. DSCarver: decompose-and-spiral-carve for subtractive manufacturing. *ACM Transactions on Graphics* 37, 4 (aug 2018), 1–14. <https://doi.org/10.1145/3197517.3201338>
- Fanchao Zhong, Wenqiang Liu, Yu Zhou, Xin Yan, Yi Wan, and Lin Lu. 2020. Ceramic 3D printed sweeping surfaces. *Computers & Graphics* 90 (aug 2020), 108–115. <https://doi.org/10.1016/j.cag.2020.05.007>
- Andrea Zocca, Paolo Colombo, Cynthia M. Gomes, and Jens Günster. 2015. Additive Manufacturing of Ceramics: Issues, Potentialities, and Opportunities. *Journal of the American Ceramic Society* 98, 7 (jul 2015), 1983–2001. <https://doi.org/10.1111/jace.13700>

A PC-MPC TO PC-TSP

The precedence constrained traveling salesman problem (PC-TSP) was formulated by [Kubo and Kasugai 1991]: "Given a directed complete graph $G(V, E)$, a distance D_{ij} on each arc $(i, j) \in E$, precedence constraints $<$ on V , find a minimum distance tour that starts node $1 \in V$, visits all the nodes in $V - \{1\}$, and returns node 1 again so that node i is visited before node j when $i < j$ ". [Kubo and Kasugai 1991] has proved PC-TSP is NP-hard. We define our precedence constrained minimum path cover problem (PC-MPC): given a directed acyclic graph $G(V, E)$ where edges are precedence constraints $<$ on V , our goal is to find a path cover for G with the fewest paths.

To prove that PC-MPC is NP-hard, we reduce this problem to PC-TSP for the input of PC-MPC G to turn it into a weighted directed complete graph: (1) set the weight of directed edges of G to 0. (2) add missing edges to make G a directed complete graph G_{com} where the weight of new edges is set to 1. Therefore, we convert the input of PC-MPC $\{G, <\}$ to the input of PC-TSP $\{G_{com}, D, <\}$ in linear time. The goals of PC-TSP and PC-MPC are equivalent by this conversion. With an arbitrary starting node meeting precedence constraints, find a tour from this node by solving PC-TSP. The output of PC-TSP can be taken as the output of PC-MPC by removing edges with weight 1 on tour. The minimum distance of PC-TSP plus is equal the number of paths for the minimum path cover of PC-MPC.

B ORIENTATION DETERMINATION CRITERIA

For the surfaces whose normal is approximately parallel to the printing orientation, insufficient sampling of slicing layers always leads to under-filling around such surface areas (see the left of Figure 13). E_{flat} is proposed to minimize such low slope areas, where θ is the angle between the triangle surface normal and the printing orientation, $\mathcal{A}(f)$ is the area of face f :

$$E_{flat} = \frac{\sum_{f \in M} |\cos \theta| \cdot \mathcal{A}(f)}{\sum_{f \in M} \mathcal{A}(f)}. \quad (1)$$

$E_{support}$ represents the ratio of the support structure volume to the total printing volume, where n is the total printing layers, $\mathcal{V}(s_i)$ and $\mathcal{V}(m_i)$ indicate the support volume and model volume of i -th layer:

$$E_{support} = \frac{\sum_{i=1}^n \mathcal{V}(s_i)}{\sum_{i=1}^n (\mathcal{V}(s_i) + \mathcal{V}(m_i))}. \quad (2)$$

C THE PSEUDO-CODE

This is a process in which depth-first search (DFS) is nested in breadth-first search (BFS). BFS builds the *solution_space_tree* (sst).

Algorithm 1 Searching based PC-MPC algorithm

```

1: Input:  $G_{init}(V, E)$ , the beam search width  $W$ 
2: Output: a set of minimal path cover with PC
3:  $indegree, visited, solution\_space\_tree$ 
4:  $solution\_space\_tree.root \leftarrow empty\ node$ 
5: add  $solution\_space\_tree.root$  to  $queue$ ,  $candidate\_paths \leftarrow \emptyset$ 
6: while  $queue \neq \emptyset \parallel candidate\_paths \neq \emptyset$  do
7:    $pre\_node \leftarrow queue.front()$ 
8:   update  $indegree, visited$  by  $pre\_node$ 
9:    $jud\_terminate \leftarrow false$ 
10:  for each  $v \in V$  do
11:    if  $indegree[v] == 0$  and  $visited[v] == false$  then
12:       $jud\_terminate \leftarrow true$ 
13:       $next\_path \leftarrow$  longest path from  $v$  with PC by DFS
14:      add  $next\_path$  to  $candidate\_paths$ 
15:  recover  $indegree, visited$ 
16:   $queue.pop()$ 
17:  if  $queue == \emptyset$  then
18:    if  $jud\_terminate == false$  then break
19:    score and sort each path of  $candidate\_paths$ 
20:     $queue \leftarrow$  top  $W$  paths of  $candidate\_paths$ 
21:    add  $queue$  to  $solution\_space\_tree$ 
22:     $candidate\_paths \leftarrow \emptyset$ 
23: return all the shortest paths from root to leaves
    of  $solution\_space\_tree$ 

```

DFS finds the path of each node on the sst (113). Before searching for next nodes from the current node in sst , we delete paths in G_{init} that have been searched from the current node to the root of sst (18). After searching the current node is over, the opposite operation needs to be done to avoid interfering next search (115). After searching all nodes is over in the current layer of sst , choose W new searched nodes to update sst (119-21). When all nodes in G_{init} are visited, we will not perform searching of the next layer (118).

Algorithm 2 OPP merging through curved layers

```

1: Input: a  $G_{OPP}(V, E)$  and sub-OPPs of each OPP node
2: Output: new  $G_{OPP}$  with less OPP nodes
3: for all pairs of nodes ( $N_1$  and  $N_2$ ) on all the edges of  $G_{OPP}$  do
4:   if TRYMERGING( $N_1, N_2$ ) == true then update  $G_{OPP}$ 
5: function TRYMERGING(node  $N_1$ , node  $N_2$ )
6:   if more than one path between  $N_1$  and  $N_2$  in  $G_{OPP}$  then
7:     return false
8:    $Set_1 \leftarrow$  all sub-OPPs of  $N_1$  and  $N_2$ 
9:    $Set_2 \leftarrow \emptyset$ 
10:  for all pairs of nodes in  $Set_1$  do
11:    if two nodes are sub-OPP of  $N_1$  and  $N_2$  respectively
    & exist edge connecting them in  $G_{init}$  then
12:      add the two nodes to  $Set_2$ 
13:  iteratively merge all pairs of nodes by curving in  $Set_2$ 
14:  if the remain nodes of  $Set_2$  can stacking into one OPP then
15:    update sub-OPPs of new node merged by  $N_1$  and  $N_2$ 
16:    return true
17:  else
18:    return false

```
